Human Factors and Ergonomics in Design, Vol. 210, 2026, 235–246
https://doi.org/10.54941/ahfe1007445

Development and Validation of a Dynamic Multi-Modal Digital Human Hand Model for Ergonomic Design of Handheld Products

Huilin Dai, Yilin Yang, and Haining Wang

School of Design, Hunan University, Changsha 410082, China

ABSTRACT

Handheld interactive products require device geometries that accommodate coupled skeletal motion and nonlinear soft-tissue deformation during grasping and pressing. However, many existing digital hand models prioritize either kinematics or surface geometry and therefore provide limited predictive power for contact mechanics and deformation under realistic interactions. This study developed a Dynamic Digital Human Hand Model (DHHM) that integrates (i) percentile-based hand surface models derived from 3D scans of 864 Chinese adults, (ii) layered internal anatomy (bone, muscle, connective tissue, fat, and skin) refined using anatomical atlases and public anatomical datasets, (iii) inverse-kinematics-driven motion control, and (iv) finite element-based soft-tissue simulation implemented in Ziva VFX using a second-order implicit backward differentiation formula (BDF2) integrator. The P50 model was validated using motion capture, 3D surface scanning, and surface electromyography (sEMG) from four participants whose hand dimensions were close to the P50 hand (maximum absolute deviation 2.0 mm across eight key measures). Participants performed seven representative grasp/press tasks involving a mouse, a laparoscopic ultrasonic scalpel, a surgical needle holder, and a smartphone. Across tasks, the DHHM reproduced primary contact patterns observed in scanned postures. Surface deviation analysis showed high agreement between simulated and scanned skin surfaces within an industrial tolerance (maximum deviation within ±1.655 mm). Predicted activation trends of thenar, hypothenar, and extensor muscle groups were qualitatively consistent with sEMG across task types. The proposed DHHM provides a validated pathway for high-fidelity hand-product interaction simulation to support ergonomic design with reduced reliance on physical prototypes.

Keywords: Digital human modeling, Hand biomechanics, Soft-tissue simulation, Inverse kinematics, Surface electromyography

INTRODUCTION

In contemporary smart product design, the hand serves as a core interaction medium enabling control through grasping, pressing, touching, and swiping. Ergonomic design for handheld products therefore requires careful consideration of hand anatomy and biomechanics to balance performance, comfort, and safety. In repetitive or precision work, neuromuscular loading and fatigue patterns are often reflected by measurable myoelectric

Received February 5, 2026; Revised April 5, 2026; Accepted April 22, 2026; Available online July 20, 2026

© 2026 The Authors. This work is licensed under a Creative Commons Attribution-NonCommercial-NoDerivatives 4.0 License.
For more information, see https://creativecommons.org/licenses/by-nc-nd/4.0/

manifestations, motivating the use of surface electromyography (sEMG) as a practical validation signal for interaction-related biomechanics (Ranavolo et al., 2018).

The human hand is structurally complex, comprising 27 bones, over 30 muscles, and numerous tendons and ligaments (Jones & Lederman, 2006). To evaluate handheld-product design across dimensions such as joint loading, muscle recruitment, and biomechanical suitability, researchers commonly employ musculoskeletal models incorporating skeletal structures, muscle paths, and finger motion mechanisms (Mirakhorlo et al., 2018; Vignais & Marin, 2014). Nevertheless, many existing models focus primarily on kinematics and simplified muscle actuation and do not explicitly represent a complete soft-tissue system (e.g., fat and skin) capable of reproducing contact-induced deformation. This limits their ability to predict contact patterns, skin deformation, and localized tissue response during dynamic grasping and pressing tasks, which is essential for fine-grained ergonomic optimization of handheld products.

To address these gaps, this study develops and validates a Dynamic Digital Human Hand Model (DHHM) that integrates population-based surface geometry, layered anatomical structures, inverse-kinematics (IK) driving, and finite-element (FE) soft-tissue simulation. The model is validated using multimodal experimental data (motion capture, scanned posture geometry, and sEMG) across representative handheld-product interaction tasks. The contribution is a reproducible modeling and validation pipeline that improves biological fidelity for hand–product interaction simulation and supports ergonomic design decisions earlier in the development cycle.

METHODS

Sample Data Acquisition for Skin-Layer Geometric Models

To ensure that the hand skin-layer model represents the surface morphology of Chinese hands, the required minimum sample size was determined following ISO 15535 (ISO 15535, 2012). Under a 95% confidence level, the minimum sample size was estimated as:

$$M = \left(1.96 \times \frac{CV}{\alpha}\right)^2$$

Where 1.96 corresponds to the 95% confidence level, CV denotes the coefficient of variation of the target dimension, α indicates the required relative accuracy, and N is the required sample size. The calculation yielded a minimum sample size of 132 individuals.

To cover China's major population centers, stratified proportional random sampling was used to recruit 864 participants aged 18–65 across six regions: East China (144), North China (151), Northeast China (150), South China (143), Northwest China (144), and Southwest China (127) (Figure 1A).

High-precision structured-light 3D scanning (Artec Eva) was used to capture right-hand surface geometry. Following established hand

anthropometry protocols (Mandahawi et al., 2008; Shahriar et al., 2020), 56 anatomical landmarks were marked prior to scanning to support robust registration and reconstruction.

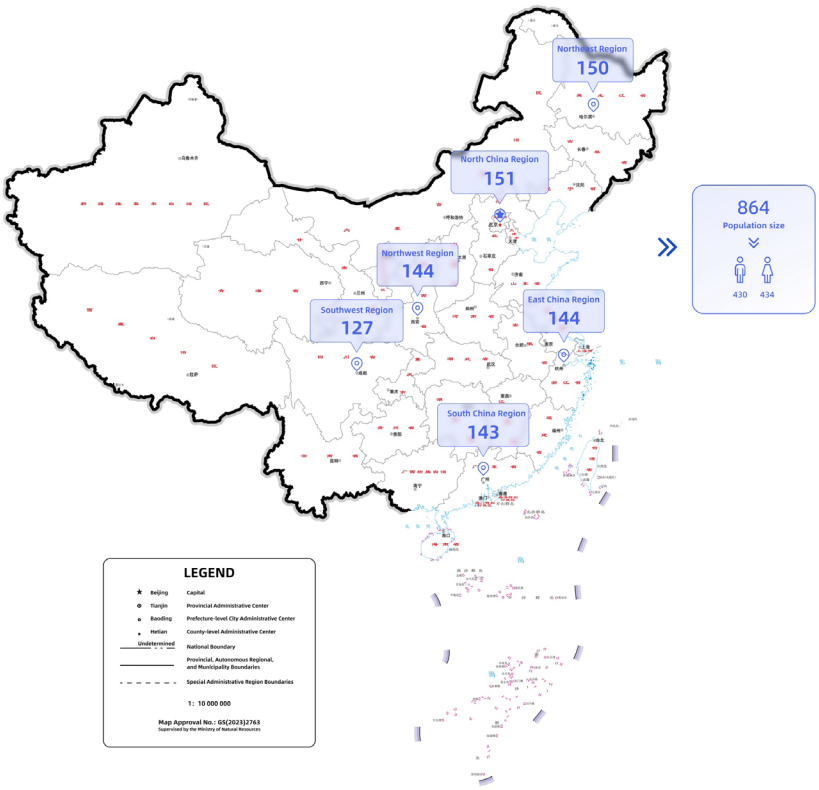

Figure 1: Distribution of the population sample.

Construction of Percentile Hand Surface Models

The captured hand data samples were converted from point cloud format to mesh format using Artec Studio 17 Professional software. A hand coordinate system was established with the midpoint of the line connecting the radial styloid process and the ulnar styloid process as the origin; the positive x-axis direction was defined as the line from the origin to the radial styloid process, and the positive z-axis direction was defined as the line from the origin to the tip of the middle finger. In Geomagic Wrap 2017, all models were sequentially processed through curvature optimization, normal reorientation, and remeshing to ensure consistent edge lengths in the target mesh and enhance the consistency of all models. Additionally, the coordinates of feature points were synchronously extracted.

Following representative approaches for parametric skin model generation (Lee et al., 2017; Lee et al., 2018), we employed bounded biharmonic weights (BBW) mesh deformation and feature-point registration/fusion algorithms to ensure accurate mesh topology correspondence across all skin surface models,

each of which consists of 88,399 triangles. Finally, in MATLAB, we sorted the models by percentile based on the Euclidean distance from the origin to the vertices of the corresponding triangular faces, and reconstructed five representative percentile surface models (P5, P25, P50, P75, P95) (Figure 2A).

In Autodesk 3ds Max, the 3D measurement values of these five percentile models were compared and calibrated against the measured statistical data of hand features, with measurement errors controlled within 0.1 mm.

Biomechanical binding and validation in this study were performed on the P50 hand skin layer. A forearm skin extension was constructed using a large-scale 3D measurement database of Chinese wrists (Chen et al., 2022), and the initial five-finger-spread pose was adjusted to a natural relaxed state (Figure 2B).

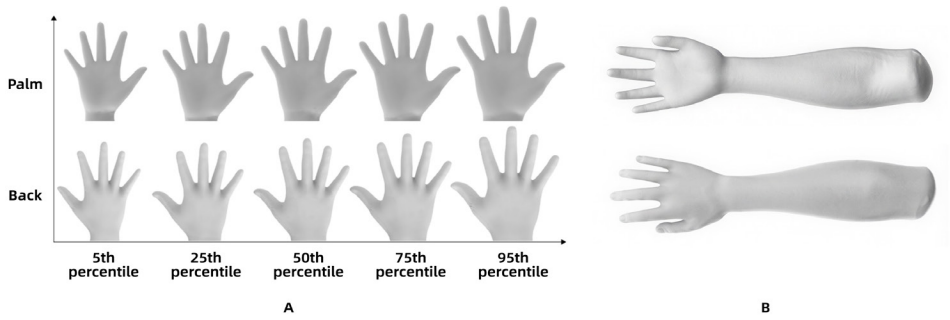

Figure 2: (A) Percentile hand skin models; (B) restored P50 skin model with forearm extension.

Layered Modeling of Skeletal, Muscular, and Connective Tissues

We used the Z-Anatomy model library as the baseline anatomical source and refined internal structures using authoritative atlases (Gray's Basic Anatomy and Sobotta Atlas of Human Anatomy) (Drake et al., 2012; Paulsen et al., 2011). Key tissues influencing skin deformation, including fat, muscles, and connective tissues, were optimized and corrected. The resulting model comprised 27 hand bones, 2 forearm bones, 1 upper-arm bone, 42 muscles, and 54 connective-tissue structures (Figure 3A). Tissue origins/insertions and anatomical layering were corrected to improve biomechanical plausibility and general anatomical consistency.

The fascial layer was not explicitly modeled. Instead, after completing skeletal, muscular, and connective-tissue modeling, a virtual shrink-wrapping (compression) procedure was applied to generate an envelope conforming to internal structures (Figure 3B). The envelope boundary was then connected to the skin layer to form a closed adipose layer that envelops the muscles (Figure 3C).

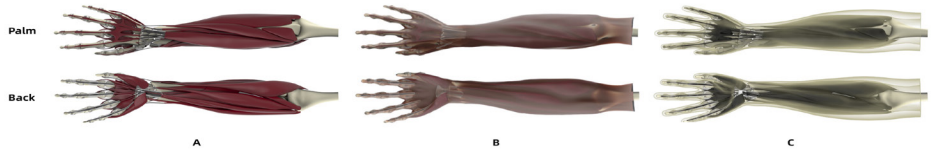

Figure 3: Repaired hand layered model: (A) skeletal, muscular, and connective tissues; (B) fascial envelope; (C) adipose layer.

Biomechanical Material Definition

Biomechanical material properties were assigned within the Maya Ziva VFX solver. M1–M42 denote the muscle belly–tendon complex; C5–C8 ligaments; C9–C18 tendon sheaths; C19 fibrous sheaths; and C20 interosseous membranes. Material parameters were referenced from biomechanics literature (Martin et al., 1998;Swedberg et al., 2014) and adaptively adjusted based on simulation stability and response.

Table 1: Material parameters for zTissue components.

Model ID	Anatomical Component	Young's Modulus (Pa)	Poisson's Ratio	Density (kg/m^3)
M1-M42	Muscle belly	2.47×10^3	0.47	1060
	Tendon	1.25×10^8	0.49	1170
C5-C8	Ligament	1.14×10^8	0.49	1120
C9-C18	Tendon sheath	1.00×10^9	0.49	1120
C19	Fibrous sheath	1.00×10^9	0.48	920
C20	Interosseous membrane	2.00×10^9	0.49	1120
-	Fat	3.00×10^5	0.49	900

Kinematic Relationship Constraints and Dynamic Simulation

Extreme-motion sequences from the ActorCore database were retargeted to the virtual hand joints to define joint limits. In Maya Ziva VFX, zAttachment constraints were used to couple muscles and connective tissues to the skeleton. Tendon-to-bone insertions were modeled as fixed attachments, while sliding attachments were applied where relative motion was expected (e.g., between muscle bellies, tendon sheaths, and tendons). Muscle contraction directions were defined using zFiber fields, and zLine-of-Action curves anchored at origin and insertion sites were used to drive fiber shortening during skeletal motion. The skin layer was defined using zCloth and coupled to the adipose layer.

Dynamic responses were solved using zSolver with a BDF2 second-order implicit integrator, producing stable soft-tissue deformation under skeleton-driven kinematics (Figure 4).

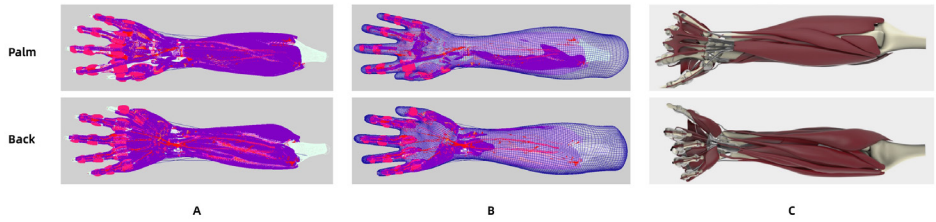

Figure 4: (A) bone, muscles and connective tissues; (B) adipose/skin coupling; (C) skeleton-driven deformation results.

EXPERIMENTAL METHODS

Participants

The P50 hand model served as the motion-driving reference. Participants were selected according to GB/T 16252-2023 to match the P50 anthropometry. Four participants were recruited, and eight key hand dimensions were measured. Across the eight dimensions in Table 2, participants were anthropometrically close to the P50 hand; the maximum absolute deviation from the P50 values was 2.0 mm, supporting validation without additional re-scaling of the reference model.

Table 2: P50 and participant hand dimensions (mm).

Participant ID	Palm Length	Hand Length	Hand Breadth	Thumb Length	Index Finger Length	Middle Finger Length	Ring Finger Length	Little Finger Length
P50	108.1	181.5	83.5	56.8	68.9	76.4	70.9	56.4
S1	107.3	183.4	81.9	58.5	70.8	77.8	70.2	57.6
S2	106.5	182.2	80.5	58.5	67.1	74.8	71.5	58.0
S3	109.7	181.1	81.2	58.2	70.6	78.3	71.6	57.3
S4	108.6	180.6	85.2	58.5	68.0	77.2	72.0	55.8

Experimental Procedure

Seven product-grasping tasks were designed (Tasks a-g), involving a mouse, a laparoscopic ultrasonic scalpel, a surgical needle holder, and a smartphone (Figure 5). These tasks covered common interaction patterns such as grasping, pressing, and precision manipulation.

Reflective markers were placed on 21 core hand joints to capture kinematics using a QUALISYS optical motion capture system (Figure 6A). sEMG measured activation patterns of the thenar eminence, hypothenar eminence,

and finger extensors (Figure 6B). After task completion in standardized postures, optical 3D scanning was used to capture hand-product postures for contact-state and geometry validation (Figure 6C).

ID	Task	Description	Product	Diagram
a	Left-click	Left-click the mouse	Mouse	
b	Grip to activate	Intraoperative grasping and cauterization of human tissue	Laparoscopic Scalpel	
c	Push apart and separate	Intraoperative retraction and dissection of human tissue		
d	Clamp and release	Intraoperative needle manipulation	Needle Holder	
e	Tap screen - portrait mode	Typing in portrait mode	Mobile Phone	
f	Tap screen - landscape mode	Taking photos in landscape mode		
g	Tap side button - portrait mode	Using side buttons to take photos in portrait mode		

Figure 5: Experimental equipment and task description.

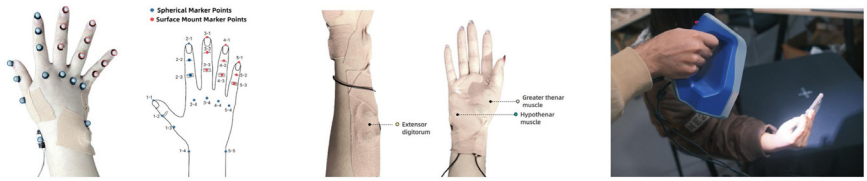

Figure 6: (A) motion-capture joints; (B) sEMG muscle groups; (C) 3D scan acquisition of hand posture.

Data Processing and Evaluation Metrics

Model accuracy was assessed in three dimensions:

1. Contact/interference distribution: motion capture drove the skeleton to target poses. Dynamic simulation yielded steady-state hand–product contact maps (Figure 7).
2. Skin deformation deviation: geometric deviation between simulated skin and scanned skin in identical poses was calculated (maximum positive/negative deviation, mean signed deviation, mean positive/negative deviation, standard deviation, and RMS). Deviation maps were visualized using a color spectrum (Table 3; Figure 8).
3. Muscle activity characteristics: model-derived fiber strain for three muscle groups was compared against experimentally collected integrated EMG (iEMG) to evaluate task specificity (Figure 9). sEMG was used as a practical physiological signature to cross-check the plausibility of simulated recruitment trends (Ranavolo et al., 2018).

Table 3: 3D deviation between simulated and scanned skin surfaces (mm).

Task	Max+	Max−	Mean	Mean+	Mean−	SD	RMS
A	1.235	−1.235	−0.102	0.295	−0.342	0.394	0.432
B	1.095	−1.092	−0.063	0.316	−0.330	0.395	0.418
C	1.155	−1.167	−0.033	0.298	−0.313	0.383	0.397
D	1.165	−1.165	−0.268	0.293	−0.317	0.383	0.395
E	1.060	−1.060	−0.099	0.301	−0.335	0.387	0.411
F	1.093	−1.093	−0.108	0.274	−0.346	0.389	0.415
G	1.655	−1.655	−0.070	0.461	−0.418	0.566	0.581
Average	1.208	−1.210	−0.106	0.320	−0.343	0.414	0.436

RESULTS

Distribution of Contact Interference Zones

The simulated contact-interference maps (Figure 7) indicate that the DHHM reproduced the main contact patterns observed in scanned postures, particularly for primary manipulative digits (thumb, index, and middle fingers). Across Tasks B-D, dominant contacts occurred at the thumb fingertip, the palmar surface, and proximal interphalangeal regions of assisting fingers. In Tasks E-G, contact concentrated at the thumb-index pinch region and palmar support area, consistent with precision manipulation and stabilization requirements.

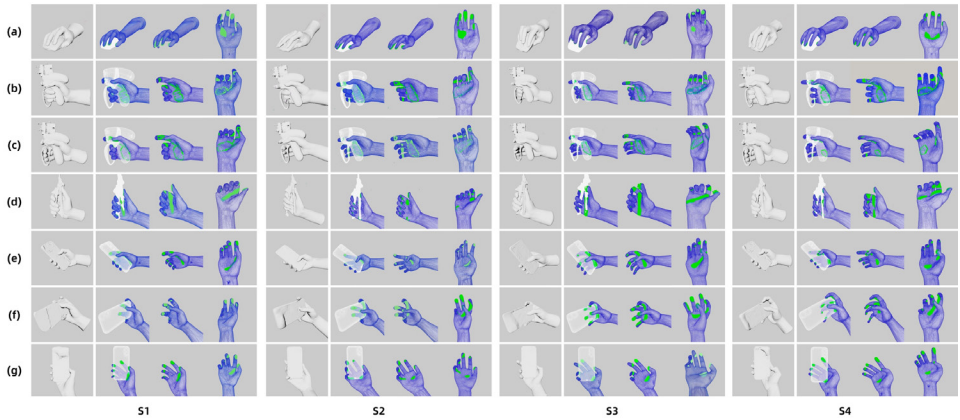

Figure 7: Scanned hand postures (left) and simulated contact states (right). Panels (a-g) correspond to Tasks a-g; columns (S1-S4) correspond to participants.

However, discrepancies were observed for auxiliary digits (ring and little fingers). Compared with scanned postures, the simulated model showed insufficient continuous contact in ring and little finger regions, whereas real hand scans exhibited more uniform multi-digit contact. This suggests that the current model may overemphasize primary digit contribution while underrepresenting stabilization roles of ulnar-side digits. Future work will focus on improving ulnar-side contact modeling and compliance.

Skin Deformation Deviation

Comparison of 3D deviations between simulated and scanned skin surfaces (Table 3; Figure 8) demonstrates excellent overall fit across tasks. The mean of the task-level maximum deviations was within ±1.208 mm, the overall mean signed deviation was -0.106 mm, and the mean SD and RMS were 0.414 mm and 0.436 mm, respectively. The maximum deviation across tasks remained within ±1.655 mm, satisfying the high-precision tolerance range of ±1.7 mm for industrial applications.

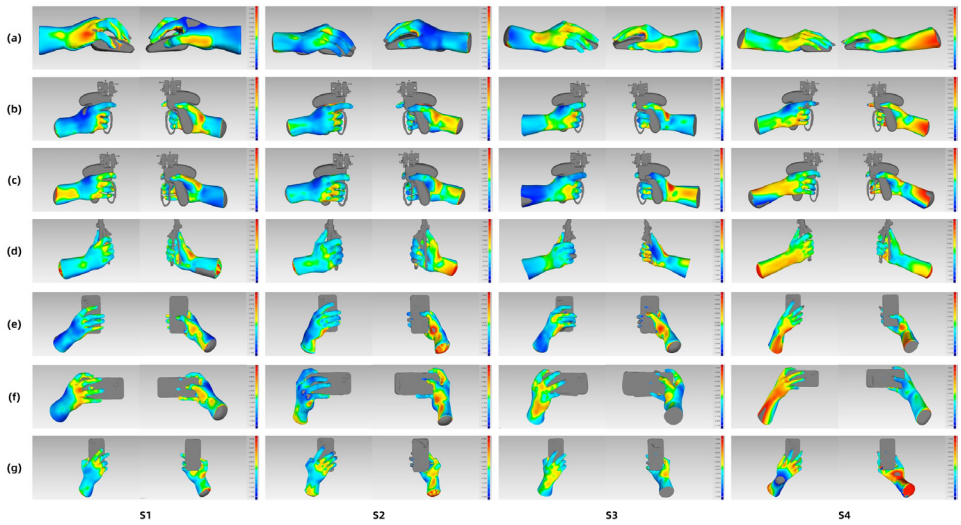

Figure 8: 3D deviation maps between simulated and scanned postures. Panels (a-g) correspond to Tasks a-g; columns (S1-S4) correspond to participants.

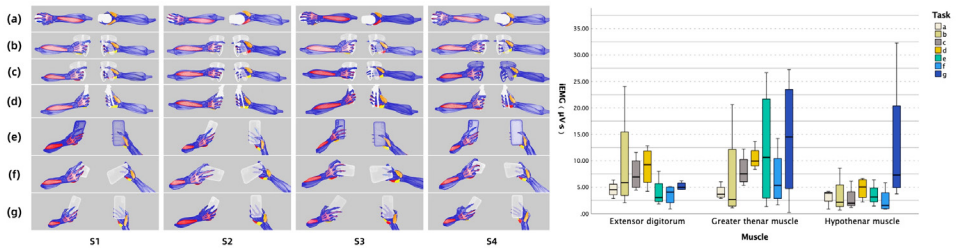

Figure 9: Model-predicted muscle activation (left) and iEMG (right) across tasks. Panels (a-g) correspond to Tasks a-g; columns (S1–S4) correspond to participants.

Deviation maps showed minimal errors (generally < 1 mm) in the forearm, dorsal fingers, and non-contact palmar regions. Larger local deviations were concentrated at fingertips, palmar bulges in high-contact areas, and dorsal stretching regions. These deviations are plausibly attributable to inter-individual variability in soft-tissue thickness and small temporal differences between scanning at sustained contact and simulation near initial contact. The observed deviation magnitudes remain within acceptable ranges for industrial design applications.

Muscle Activity Characteristics

Simulation and experimental data indicate that predicted muscle activation trends generally aligned with sEMG across tasks. In Task A, both simulation and sEMG showed relatively low activation across muscle groups. In Task B, involving stable thumb grip and index pressing, higher activation was observed in thenar muscles and finger extensors, consistent with measured trends. In Tasks C and D, which required resistance and stabilization control, the model predicted sustained higher activation in thenar muscles and extensors, again consistent with measured demands. In Tasks E and F dominated by thumb flexion/extension, the model predicted higher thenar activity, broadly matching experimental trends. In Task G, which combined thumb motion with ulnar-side stabilization, both thenar and hypothenar activation were elevated, aligning with sEMG patterns.

Overall, the DHHM captured task-dependent coordination strategies: precision manipulation tasks (A, E, F, G) showed coordinated thenar-hypothenar recruitment, whereas forceful grasp/press tasks (B, C, D) emphasized extensor-related activation. Prediction quality varied by muscle group; superficial groups with clearer anatomical structures were more reliably characterized, while deep intrinsic muscle synergies remain challenging due to complex architecture and transmission mechanisms.

DISCUSSION

This study integrates a hand anthropometry database, kinematic data acquisition, and an embedded FE simulation engine to construct an industry-oriented dynamic digital hand model incorporating skeletal, muscular, soft tissue, and skin layers. By combining population-based skin surfaces with anatomically refined internal structures, the DHHM supports realistic skeleton-driven deformation and contact behavior during handheld-product interaction.

Validation results indicate that the model reproduces primary-digit contact patterns with high consistency relative to scanned postures, and skin surface agreement is within a high-precision tolerance range. In addition, task-dependent muscle activation trends were qualitatively consistent with sEMG, supporting biomechanical plausibility for key muscle groups (Ranavolo et al., 2018). Importantly, the observed discrepancies for ring and little fingers highlight that ulnar-side stabilization mechanics are a primary target for refinement, especially for grasps requiring distributed multi-digit contact.

From an ergonomic design perspective, the proposed framework provides a digital carrier for refined analysis and product optimization, enabling designers to identify potential biomechanical risks earlier in the development process and reducing reliance on repeated physical prototyping.

Limitations and Future Work

Three limitations should be noted. First, the current validation focused on four participants selected to be close to the P50 hand; generalization across hand sizes and percentiles will require additional validation. Second, contact

discrepancies in the ring and little fingers indicate that ulnar-side digit stabilization mechanics require refinement. Third, deeper intrinsic muscle coordination remains difficult to represent using the current simplifications of muscle architecture and transmission; improved muscle modeling and additional physiological measurements may strengthen prediction fidelity.

CONCLUSION

A dynamic digital human hand model integrating anthropometric surface models, layered anatomy, inverse-kinematics control, and finite element soft-tissue simulation was developed and validated. Comparative experiments using motion capture, 3D scanning, and sEMG indicate that the model reproduces realistic contact patterns and skin deformation within an industrial tolerance and captures task-dependent activation trends of key muscle groups. The proposed DHHM provides a validated pathway for high-fidelity hand-product interaction simulation to support ergonomic optimization of handheld products and reduce reliance on physical prototypes.

ACKNOWLEDGMENT

The authors would like to express their gratitude to the staff of the Anthropometry and Wearables Design Lab at Hunan University for their technical support and for providing the experimental facilities. Special thanks are given to the participants involved in this study.

REFERENCES

Chen, Q., Wang, H., & Liu, K. (2022). Anthropometric Hand Dimensions of Chinese Adults Using Three-Dimensional Scanning Technique. *Lecture Notes in Computer Science*,pp. 377–387.

Drake, R., Vogl, A., & Mitchell, A. (2012). Gray's Basic Anatomy.

ISO 15535. (2012). General requirements for establishing anthropometric databases. International Organization for Standardization.

Jones, L., & Lederman, S. (2006). Human Hand Function.

Lee, W., Goto, L., Molenbroek, J., & Goossens, R. (2017). Analysis methods of the variation of facial size and shape based on 3D face scan images. Proceedings of the human factors and ergonomics society annual meeting, Vol. 61, No. 1, pp. 1409–1413.

Lee, *W., Kim, J. G., Molenbroek, J., Goossens, R*., Jung, H., & You, H. (2018). Contact Pressure Analysis for Wearable Product Design. Advances in Intelligent Systems and Computing.

Mandahawi, N., Imrhan, S., Al-Shobaki, S., & Sarder, B. (2008). Hand anthropometry survey for the Jordanian population. *International Journal of Industrial Ergonomics*, *38*(11-12),pp. 966–976.

Martin, R. B., Burr, D. B., & Sharkey, N. A. (1998). Mechanical Properties of Ligament and Tendon. *Springer New York*.

Mirakhorlo, M., Van Beek, N., Wesseling, M., Maas, H., Veeger, H. E. J., & Jonkers, I. (2018). A musculoskeletal model of the hand and wrist: model definition and evaluation. *Computer methods in biomechanics and biomedical engineering*, *21*(9-12),pp. 548–557.

Paulsen, F., Waschke, J., Klonisch, T., & Hombach-Klonisch, S. (2011). Sobotta - Atlas of Human Anatomy, General anatomy and musc*uloskeletal system*.

Ranavolo, A., Chini, G., Silvetti, A., Mari, S., Serrao, M., & Draicchio, F. (2018). Myoelectric manifestation of muscle fatigue in repetitive work detected by means of miniaturized sEMG sensors. Int J Occup Saf Ergon, 24(3),pp. 464–474.

Shahriar, M. M. P., Parvez, M. S., & Lutfi, M. S. (2020). A survey of hand anthropometry of Bangladeshi agricultural farm workers. International Journ*al of Industrial Ergonomi*cs, 78, 102978.

Swedberg, A. M., Reese, S. P., Maas, S. A., Ellis, B. J., & Weiss, J. A. (2014). Continuum description of the Poisson's ratio of lig*ament and tendon under finite deformation*. *Jou*rnal of Biomechanics, 47(12), 3201–3209.

Vignais, N., & Marin, F. (2014). Analysis of the musculoskeletal system of the hand and forearm during a cylinder grasping task. International Journ*al of Industrial Ergono*mics, 44(4), 535–543.